Title
Kinome Reprogramming Is a Targetable Vulnerability in ESR1 Fusion-Driven Breast Cancer.

Journal
Cancer Research, 83(19)

Authors
Kim, Beom-Jun
Anurag, Meenakshi
Lei, Jonathan
et al.

Publication Date
2023-10-02

DOI
10.1158/0008-5472.CAN-22-3484

Peer reviewed

Kinome Reprogramming Is a Targetable Vulnerability in ESR1 Fusion-Driven Breast Cancer

Xuxu Gou[1,2,3], Beom-Jun Kim[1,4], Meenakshi Anurag[1,4], Jonathan T. Lei[1,5], Meggie N. Young[1,6], Matthew V. Holt[1], Diana Fandino[1], Craig T. Vollert[1,7], Purba Singh[1], Mohammad A. Alzubi[7], Anna Malovannaya[6], Lacey E. Dobrolecki[1], Michael T. Lewis[1,8,9,10], Shunqiang Li[11], Charles E. Foulds[1,4,9], and Matthew J. Ellis[1,2,4,8,9]

ABSTRACT

Transcriptionally active ESR1 fusions (ESR1-TAF) are a potent cause of breast cancer endocrine therapy (ET) resistance. ESR1-TAFs are not directly druggable because the C-terminal estrogen/anti-estrogen–binding domain is replaced with translocated in-frame partner gene sequences that confer constitutive transactivation. To discover alternative treatments, a mass spectrometry (MS)–based kinase inhibitor pulldown assay (KIPA) was deployed to identify druggable kinases that are upregulated by diverse ESR1-TAFs. Subsequent explorations of drug sensitivity validated RET kinase as a common therapeutic vulnerability despite remarkable ESR1-TAF C-terminal sequence and structural diversity. Organoids and xenografts from a pan-ET–resistant patient-derived xenograft model that harbors the ESR1-e6>YAP1 TAF were concordantly inhibited by the selective RET inhibitor pralsetinib to a similar extent as the CDK4/6 inhibitor palbociclib. Together, these findings provide preclinical rationale for clinical evaluation of RET inhibition for the treatment of ESR1-TAF–driven ET-resistant breast cancer.

Significance: Kinome analysis of *ESR1* translocated and mutated breast tumors using drug bead-based mass spectrometry followed by drug-sensitivity studies nominates RET as a therapeutic target.

See related commentary by Wu and Subbiah, p. 3159

Introduction

Multiple *ESR1* fusion genes generated by chromosomal translocation have recently been identified in biopsy samples from estrogen receptor alpha–positive (ERα$^+$) patients with metastatic breast cancer. The prevalence of *ESR1* fusions identified to date varies between different datasets, overall occurring in 1% to 10% in ERα$^+$ breast cancers. Our group previously revealed 2 out of 25 (8%) specimens from treatment-refractory, advanced breast tumors harboring *ESR1* fusions (1). Hartmaier and colleagues (2) estimated at least 1% *ESR1* fusions in their metastatic solid breast cancer cohort. A frequency of approximately 5.4% (3/55) was observed in the MET500 study (3). Priestley and colleagues (4) reported 1.7% (7/410) in metastatic breast cancers, similar to 1.6% evaluated by Heeke and colleagues (5). The Metastatic Breast Cancer Project identified 1% (4/379) in late-stage patients (https://mbcproject.org/). Brett and colleagues (6) reported 1% to 10% in hormone receptor–positive breast cancers. Of note, in-frame pathogenic *ESR1* fusions are strongly enriched in metastatic ERα$^+$ tumors post endocrine therapy (ET) treatment. Advances in RNA sequencing (RNA-seq) technologies as a clinical tool, and the growing interest in the study of chromosomal translocations involving *ESR1*, will facilitate the accurate determination of *ESR1* fusion frequency.

Transcriptionally active ESR1 fusions (ESR1-TAF) consist of *ESR1* exons 1 to 6 (ESR1-e6) fused in-frame to C-terminal sequences from diverse 3′ gene partners (1, 7). We recently functionally characterized 15 examples and identified ten ESR1-TAFs that drive estradiol (E2)-independent cell growth, motility, invasion, epithelial-to-mesenchymal transition and pan-ET resistance (7). There are no targeted treatment options for tumors expressing ESR1-TAFs as the ligand-binding domain (LBD) is absent. There is therefore an urgent need to develop new treatments for *ESR1* gene fusion-driven tumors based on common biological features, despite C-terminal diversity.

Multiple clinical trials have evaluated the potential benefits of drugs targeting oncogenic kinases in patients who have developed ET resistance (8–10). However, the only tyrosine kinase inhibitor (TKI) class approved in this setting targets ErbB2/HER2 (11). To study the therapeutic potential of kinase inhibition more broadly, we developed a kinase inhibitor pulldown assay (KIPA) that deploys multiple small-molecule kinase inhibitors conjugated to sepharose beads to enrich for kinases before identification and quantification by mass

[1]Lester and Sue Smith Breast Center, Baylor College of Medicine, Houston, Texas. [2]Graduate Program in Translational Biology and Molecular Medicine, Baylor College of Medicine, Houston Texas. [3]UCSF Helen Diller Family Comprehensive Cancer Center, University of California San Francisco, San Francisco, California. [4]Department of Medicine, Baylor College of Medicine, Houston, Texas. [5]Department of Human and Molecular Genetics, Baylor College of Medicine, Houston, Texas. [6]Department of Biochemistry and Molecular Biology, Baylor College of Medicine, Houston, Texas. [7]Employee of Adrienne Helis Malvin Medical Research Foundation, New Orleans, Los Angeles. [8]Department of Molecular and Cellular Biology, Baylor College of Medicine, Houston, Texas. [9]Dan L. Duncan Cancer Center, Baylor College of Medicine, Houston, Texas. [10]Department of Radiology, Baylor College of Medicine, Houston, Texas. [11]Division of Oncology, Department of Internal Medicine, Washington University School of Medicine, St. Louis, Missouri.

Current address for B.-J. Kim: Translational Medicine, Oncology R&D, AstraZeneca PLC, Gaithersburg, Maryland and M.J. Ellis: Early Oncology, AstraZeneca PLC, Gaithersburg, Maryland.

X. Gou and B.-J. Kim contributed equally as co-authors of this article.

Corresponding Authors: Charles E. Foulds, Lester and Sue Smith Breast Center, Baylor College of Medicine, One Baylor Plaza, Houston, TX 77030. E-mail: foulds@bcm.edu; and Matthew J. Ellis, AstraZeneca PLC, Jose Baselga Building, One MedImmune Way, Gaithersburg, MD 20878. E-mail: Matthew.Ellis@astrazeneca.com

Cancer Res 2023;83:3237–51

doi: 10.1158/0008-5472.CAN-22-3484

spectrometry (MS; bioRxiv 2022.10.13.511593). In an initial screen, we analyzed T47D ERα$^+$ breast cancer cells transduced with expression vectors for both transcriptionally active and inactive ESR1 fusions. Subsequently, a panel of 22 independent patient-derived xenograft (PDX) tumors derived from patients with ERα$^+$ breast cancer with wild-type *ESR1* and those harboring a spectrum of *ESR1* mutations was examined. To further define targetable proteins and pathways, the KIPA results were complemented with additional PDX proteogenomic data, including whole exome sequencing, RNA-seq, MS-based proteomics, and phosphoproteomics (12–14). Furthermore, to facilitate more rapid and cost-effective drug testing, we complemented the study of the *in vivo* therapeutic response of ERα$^+$ PDX models to TKI with counterpart organoids grown *ex vivo*. This allowed a determination of whether organoids recapitulate the kinase expression patterns and therapeutic responses observed when the counterpart PDX was grown *in vivo*.

Materials and Methods

Cell culture

All cell lines were obtained from the Tissue Culture Core at Baylor College of Medicine (BCM) in 2017 from the ATCC, with validation by short tandem repeat testing completed at the Cytogenetics and Cell Authentication Core at MD Anderson. Cells were cultured at 37°C in 5% CO_2 and were tested for *Mycoplasma* every 6 months. Cell lines after passage 20 were discarded. T47D (ATCC cat# HTB-133, RRID: CVCL_0553) and MCF7 (ATCC cat# HTB-22, RRID: CVCL_0031) cells were grown in RPMI-1640 with L-glutamine (Corning, cat# 10–040-CV) supplemented with 10% FBS (Sigma-Aldrich, cat# F8067), glucose at 4.5 g/L (Sigma, cat# G5767), 10 mmol/L HEPES (GenDEPOT, cat# CA011), 1 mmol/L sodium pyruvate (GenDEPOT, cat# CA017), and 50 μg/mL gentamycin (GenDEPOT, cat# CR003–001). For hormone deprivation, cells were plated in culture media overnight, washed with Dulbecco's PBS, and maintained in phenol red-free, RPMI media (Thermo Fisher Scientific, cat# 11835) containing 10% charcoal-stripped serum (Sigma, cat# F6765) as supplemented as above (CSS media). CSS media were changed every 2–3 days for one-to-two weeks. Water-soluble E2 was purchased from Sigma (E4389).

Stable cell lines expressing YFP, truncated ESR1-e6, ESR1-WT, ESR1-Y537S, ESR1-D538G, ESR1-e6>YAP1, ESR1-e6>PCDH11X, ESR1-e6>DAB2, ESR1-e6>GYG1, ESR1-e6>SOX9, ESR1-e6>ARNT2-e18, ESR1-e6>PCMT1 and ESR1-e6>ARID1B, ESR1-e6>ARNT2-e2, ESR1-e6>LPP, ESR1-e6>NCOA1, ESR1-e6>TCF12, ESR1-e6>CLINT1, ESR1-e6>GRIP1 and ESR1-e6>TNRC6B were previously described (7).

Immunoblotting

Cells were harvested by scraping in cold PBS. Cell pellets were resuspended in either RIPA lysis buffer (Thermo Fisher Scientific, cat# 89900) for immunoblotting or MIB lysis buffer (50 mmol/L HEPES (pH 7.5), 150 mmol/L NaCl, 1 mmol/L EDTA, 1 mmol/L EGTA with 0.5% Triton X-100) supplemented with 1x protease inhibitors and 1x phosphatase inhibitors for KIPA, and lysed on ice for 30 minutes or sonicated for 2 minutes on a Covaris sonicator, respectively. Cell lysates were clarified by centrifugation at 20,000 × *g* for 30 minutes at 4°C. To make ER$^+$ PDX tumor lysates, frozen tumors were cryopulverized with a Covaris CP02 Pulverizer and then protein was extracted in MIB lysis buffer with sonication. Protein concentrations were determined by Bradford assay (Bio-Rad). Proteins (20 μg) were mixed with LDS Sample Buffer (Invitrogen, cat# NP0007), separated on 4% to 12% gradient gels (Thermo Fisher Scientific), and transferred to nitrocellulose membranes. Primary antibodies used for immunoblotting were as follows: N-terminal ERα (Millipore, cat# 04–820; RRID: AB_1587018, 1:1000), RET (Cell Signaling Technology, cat# 14556S, RRID:AB_2798509, 1:1,000), IGF1Rβ Antibody (Cell Signaling Technology, cat# 3027S, RRID:AB_2122378, 1:1,000), JAK1 (Cell Signaling Technology, cat# 29261, RRID:AB_2798972, 1:1,000), FGFR3 (Cell Signaling Technology, cat# 4574, RRID:AB_2246903, 1:1,000), FGFR4 (Cell Signaling Technology, cat# 8562, RRID:AB_10891199, 1:1,000), Phospho-p44/42 MAPK (Erk1/2; Thr202/Tyr204; Cell Signaling Technology, cat# 4370, RRID:AB_2315112, 1:2,000), total p44/42 MAPK (Erk1/2; Cell Signaling Technology, cat# 9102, RRID: AB_330744, 1:1,000), Phospho-Rb (Ser780; Cell Signaling Technology, cat# 8180S, RRID:AB_10950972, 1:1,000), total Rb (Cell Signaling Technology, cat# 9309, RRID:AB_823629, 1:2,000), Ret (pY1062) antibody (Abcam, cat# ab51103, RRID:AB_870738, 1:500), GFRα-1 antibody (Santa Cruz Biotechnology, cat# sc-271546, RRID: AB_10649373, 1:1,000), and GAPDH (Santa Cruz Biotechnology, cat# sc-47724, RRID: AB_627678, 1:5,000). The following horseradish peroxidase–conjugated secondary antibodies (anti-rabbit IgG, Cell Signaling Technology cat# 7074, RRID: AB_2099233, 1:10,000); anti-mouse IgG (Cell Signaling Technology cat# 7076, RRID: AB_330924, 1:10,000) were used and membranes were developed using ECL Detection Reagent (Thermo Fisher Scientific, cat# RPN2235) with visualization on a Bio-Rad Imaging System.

Cell growth assay

Hormone-deprived stable cells were plated in 96-well plates (3,000 cells/well). One day after plating, cells were treated as described in the figure legends. CSS media containing drugs were changed every 2 to 3 days. Cell growth was quantified using an alamarBlue reagent (resazurin sodium salt, Sigma, R7017, 0.25 mg/mL) after 7 to 10 days of treatment, and the plates were read by taking the ratio of 540 nm (λExcitation)/ 590 nm (λEmission) with a fluorescent microplate reader (BMG LABTECH). Cell growth reading values were normalized to that of control YFP cells minus E2 (−E2).

ERα$^+$ PDX models

The 22 PDX models were previously described (7, 15). All animal procedures were approved by the Institutional Animal Care and Use Committee at BCM (protocol# AN-6934). Additional information on the BCM and HCI PDX models is available at pdxportal.research.bcm.edu/ and published in (15, 16).

For drug therapeutic studies, single cells were prepared from PDX tumors. Tumors were collected from mice, chopped using a razor blade, incubated in tumor digestion solution (DMEM/F12 media, 5% FBS, 1X collagenase, 1X hyaluronidase) with rotation at 37°C for one-to-two hours. Tumor suspension was centrifuged at 1,000 rpm for 10 minutes and supernatants were removed. Red blood cell lysis buffer (Invitrogen, cat# 00–4333–57) was added and mixed. HF buffer [Hanks' Balanced Salt Solution media (Gibco, cat# 14025–092)], 2% FBS, penicillin–streptomycin (P/S, Sigma, cat# P4333) was then added to stop the lysis followed by centrifugation for 5 minutes at 1,000 rpm. Tumor cell pellets were resuspended and mixed with prewarmed 0.05% trypsin + EDTA for digestion. HF buffer was added to stop the digestion, and tumor cells were filtered through a 100-μm filter. PDX single cells were centrifuged again at 1,000 rpm for 5 minutes and resuspended in HF buffer at 5×10^5 cells in 100 μL. An equal volume of Matrigel (Corning, cat# 356255) was then added. The 200 μL mix was then injected into the fat pad of 3 to 4-week-old female SCID/beige mice (strain C.B-17/IcrHsd-Prkdc^{scid}Lyst$^{bg\text{-}J}$ from Envigo). Tumor volumes were measured by caliper every 3–4 days and were calculated

by $V = 4/3 \times \pi \times (\text{width}/2)^2 \times (\text{length}/2)$. When tumors reached around 200 mm^3, mice were randomized to receive vehicle, pralsetinib (ChemieTek, cat# CT-BLU667), palbociclib (MedChem Express, cat# HY50767), or combo containing chow diets ($n = 5$–8 per PDX line per arm). All drug-containing chow pellets were manufactured by Research Diets, Inc. Mice were sacrificed when tumors reached 1.5 cm^3 or at the study end point. Tumors were harvested and snap-frozen in liquid nitrogen for storage.

PDX organoids

Single cells isolated from PDX tumors were suspended in HF buffer and depleted for mouse stromal cells using a Mouse Cell Depletion Kit (MACS, cat# 130104694). Cells were embedded with Matrigel and plated at the concentration of 1,200 cells as per 2.5-μL organoid domes in 96-well plates. After organoid domes solidified, 90 μL of breast cancer organoid medium (defined in ref. 17) was added for overnight incubation. One day after plating, 90 μL media containing a gradient dilution of drugs as described previously in the figure legends was added and replaced every 3–4 days for one-to-two weeks. Organoids were digested using 1 U/mL dispase (STEMCELL Technologies, cat# 07923) and the growth was quantified using a CellTiter-Glo 3D Cell Viability Assay (Promega, G9682). Alternatively, PDX cells transduced with lentivirus expressing a GFP-luciferase reporter (System Biosciences, cat# BLIV101PA-1) were plated as organoids and treated as described in the figure legends. After drug treatment, luciferin (GOLDBIO, cat# LUCK-1G) was added to the organoids in growth media and the growth was quantified by counting photons produced by the luciferase enzyme using an IVIS imaging system.

KIPA

Kinase inhibitors

Palbociclib, crizotinib, GSK690693, and AZD4547 were purchased from Selleckchem. CZC-8004 was purchased from Med Chem 101. Modified afatininb, FRAX597, abemaciclib, and axitinib (containing an amino side chain for coupling) were custom synthesized by Med Chem 101.

Kinobeads preparation

For hm9KiP beads, nine kinase inhibitors (palbociclib, crizotinib, GSK690693, AZD4547, CZC-8004, afatinib, FRAX597, abemaciclib, and axitinib) were conjugated to ECH Sepharose 4B via carbodiimide coupling chemistry as previously described (bioRxiv 2022.10.13.511593). We synthesized our own ECH Sepharose 4B by conjugating 6-Aminohexanoic acid (Sigma) to cyanogen bromide (CNBr)-activated Sepharose 4B (GE Healthcare) according to the manufacturer's recommendation. Briefly, excess 6-Aminohexanoic acid was coupled to swollen CNBr-activated Sepharose 4B in 0.1 mol/L $NaHCO_3$, pH 8.3 and 500 mmol/L NaCl at 4°C overnight with rotation. Unreacted CNBr groups were then inactivated by incubating the beads with 0.1 mol/L Tris-HCl, pH 8.0 for 2 hours. The beads were then washed with five cycles of alternating low pH buffer (0.1 mol/L sodium acetate, pH 4.0 with 500 mmol/L NaCl) and high pH buffer (0.1 mol/L Tris-HCl, pH 8.0 with 500 mmol/L NaCl). Conjugation of the drugs to the laboratory-generated ECH Sepharose 4B beads was performed according to protocol described in (bioRxiv 2022.10.13.511593). Briefly, the beads were conditioned by multiple washes with 50% dimethyformamide/ethanol (DMF/EtOH). Each drug was dissolved in 50% DMF/EtOH and added to the conditioned beads in the presence of 0.1 mol/L 1-ethyl-3-(3-dimethylaminopropyl)carbodiimide (EDC) and allowed to react overnight at 4°C with rotation. After coupling, unreacted groups were inactivated with 0.1 mol/L EDC, 1 mol/L ethanolamine in 50% DMF/EtOH for 1 hour at room temperature. Subsequently, beads were washed with 50% DMF/EtOH and alternating washes of 0.1 mol/L Tris-HCl, pH 8.3 with 500 mmol/L NaCl and 0.1 mol/L acetate, pH 4.0 with 500 mmol/L NaCl.

For 5KiPv2 beads, five kinase inhibitors (palbociclib, GSK690693, AZD4547, CZC-8004, and axitinib) were conjugated to ECH-Agarose (G-Biosciences) via carbodiimide coupling chemistry (18) with minor modifications.

Kinase enrichment by kinobeads precipitation

Native cell or tumor lysates were made in MIB lysis buffer defined above supplemented with 1x protease inhibitor cocktail (Roche), 10 mmol/L NaF, 2.5 mmol/L Na_3VO_4 and 1% each of phosphatase inhibitor cocktail 2 and 3 (Sigma) by incubation on ice for 10 minutes, two-minute sonication for each sample, and then 15,000 rpm centrifugation for 20 minutes for clarification. Supernatants were collected and stored at −80°C after being snap-frozen with liquid nitrogen.

KIPA was performed as described previously (bioRxiv 2022.10.13.511593). For each KIPA pulldown, 100 μg of native lysate was mixed with 10 μL of kinobeads that were previously equilibrated in a lysis buffer for 1 hour at 4°C with rotation. Kinobeads and bound proteins were pulled down by centrifugation at 600 × *g* for 30 seconds; the supernatant containing unbound proteins were aspirated. Next, the beads were briefly washed successively two times with 400 μL wash buffer (50 mmol/L HEPES (pH 7.5), 600 mmol/L NaCl, 1 mmol/L EDTA, 1 mmol/L EGTA with 0.5% Triton X-100) and twice with the same buffer lacking Triton X-100 followed by two washes with MS-grade water (Fisher Chemical). After the final centrifugation, all the excess liquid was aspirated off and final beads were resuspended in 30 μL of 100 mmol/L NH_4HCO_3 and heated at 65°C for 10 minutes. MS grade trypsin (250 ng) was then directly added to the beads and bicarbonate mixture and digested overnight at 37°C. To remove the remaining detergent before MS analysis, the digested peptide mixture was processed using the HiPPR Detergent Removal Kit (Thermo Fisher Scientific) according to the manufacturer's directions and dried by speed-vacuum before MS analysis. hm9KiP beads were used for T47D cell experiments in **Fig. 1A**, whereas 5KiPv2 beads were used for all other experiments.

MS-parallel reaction monitoring

Targeted MS analysis was performed as previously described (bioRxiv 2022.10.13.511593). Digested peptides were analyzed on an Orbitrap Fusion Lumos Tribrid Mass Spectrometer coupled with EASY-nLC 1200 system (Thermo Fisher Scientific) for parallel reaction monitoring (PRM). One fourth of peptides from KIPA beads was loaded to a trap column (150 μmol/L × 2 cm, particle size 1.9 μmol/L) with a max pressure of 280 bar using Solvent A (0.1% formic acid in water), then separated on a silica microcolumn (150 μmol/L × 5 cm, particle size, 1.9 μmol/L) with a gradient of 5%–28% mobile phase B (90% acetonitrile and 0.1% formic acid) at a flow rate of 750 nL/min for 75 minutes. Both data-dependent acquisition (DDA) and PRM mode were used in parallel. For DDA scan, a precursor scan was performed in the Orbitrap by scanning m/z 300–1,200 with a resolution of 120,000. The most 20 intense ions were isolated by Quadrupole with a 2 m/z window and fragmented by higher energy collision dissociation (HCD) with normalized collision energy of 32% and detected by ion trap with rapid scan rate. Automatic gain control targets were 5×10^5 ions with a maximum injection time of 50 ms for precursor scans and 10^4 with a maximum injection time of 50 ms for MS2 scans. Dynamic exclusion time was 20 seconds (±7 ppm). For PRM scan, preselected peptides were isolated by quadrupole followed by HCD with normalized collision energy of 30% and product ions (MS2) were scanned by

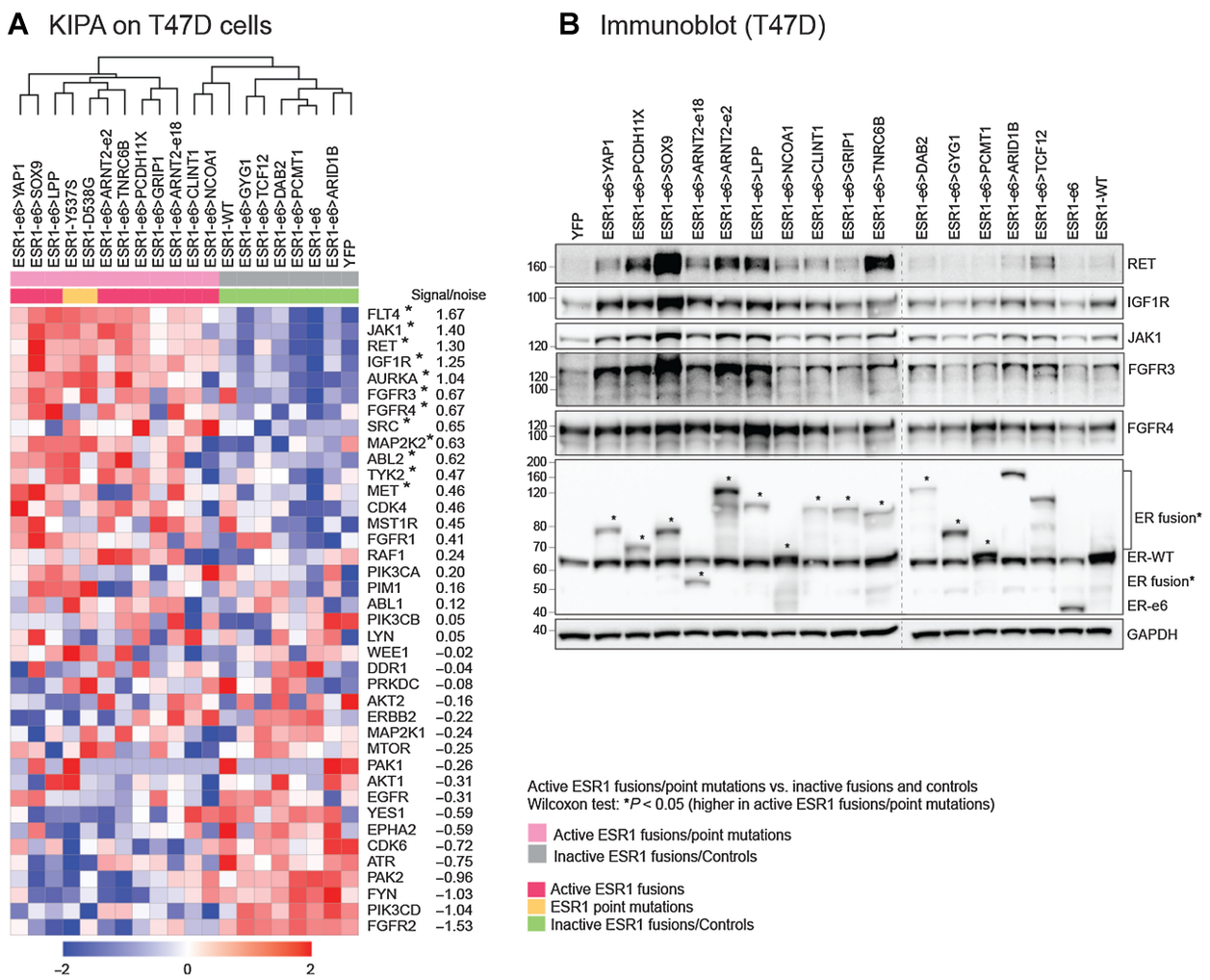

Figure 1.

KIPA profiling reveals druggable kinase expression levels induced by ESR1-TAFs in T47D breast cancer cells. **A,** Heatmap showing the expression of kinases in T47D cells expressing ESR1 fusion proteins and ERα LBD point mutants. Kinase expression values were $\log_2$ transformed. Signal/noise ratio was computed by dividing the difference of the means of TAFs and LBD mutations and inactive fusions and controls by the sum of their SDs. Scale bar indicates row Z scores (from dark blue as −2 to dark red at +2). **B,** Immunoblotting of kinases and endogenous ERα and ESR1 fusion proteins in lysates made from E2-deprived stable T47D cells. Asterisks indicate ESR1 fusion proteins. GAPDH served as a loading control. The dashed line indicates two separate blots that were conducted at the same time. Representative data are shown from two independent experiments.

Orbitrap with a resolution of 30,000. Scan windows were set to 4 minutes for each peptide. For relative quantification, the raw spectrum file was searched with Mascot, and resulting mgf output was imported to Skyline with raw spectrum. Six strongest product ions were used to calculate peptide area. For accurate quantification, all AUC ranges were manually adjusted, and nonspecific product ion was excluded. The sum of the area of product ions for each peptide was used to quantify each protein. Protein levels were median normalized, and log transformed for further analysis. For **Figs. 2B**, **3**, and **4**, proteins from KIPA were quantified by the SureQuant method using heavy-labeled peptides (bioRxiv 2022.10.13.511593).

Competition KIPA

For competition KIPA, 50 μg of T47D YFP control or T47D ESR1-e6>YAP1 lysates were incubated with DMSO or kinase inhibitors at increasing concentration (100 nmol/L, 1 μmol/L, and 10 μmol/L) for 30 minutes and mixed with 10 μL of kinobeads that have been previously equilibrated in lysis buffer for 1 hour at 4°C with rotation. Kinobeads and bound proteins were pulled down by centrifugation at 600 × *g* for 30 seconds, with the supernatant containing unbound proteins aspirated and discarded. The beads were briefly washed two times with 400 μL wash buffer (described above) and twice with the same buffer lacking Triton X-100, and finally by two washes with MS-grade water. After the final centrifugation, all excess liquid was aspirated off and beads were resuspended in 30 μL of 100 mmol/L NH_4HCO_3 and heated at 65°C for 10 minutes. On-bead digestion was carried out by adding 250 ng of trypsin directly to the beads in the bicarbonate buffer and digested overnight at 37°C. To remove the remaining detergent before MS analysis, the digested peptide mixture was processed using the HiPPR Detergent Removal Kit and dried by speed-vacuum before MS analysis.

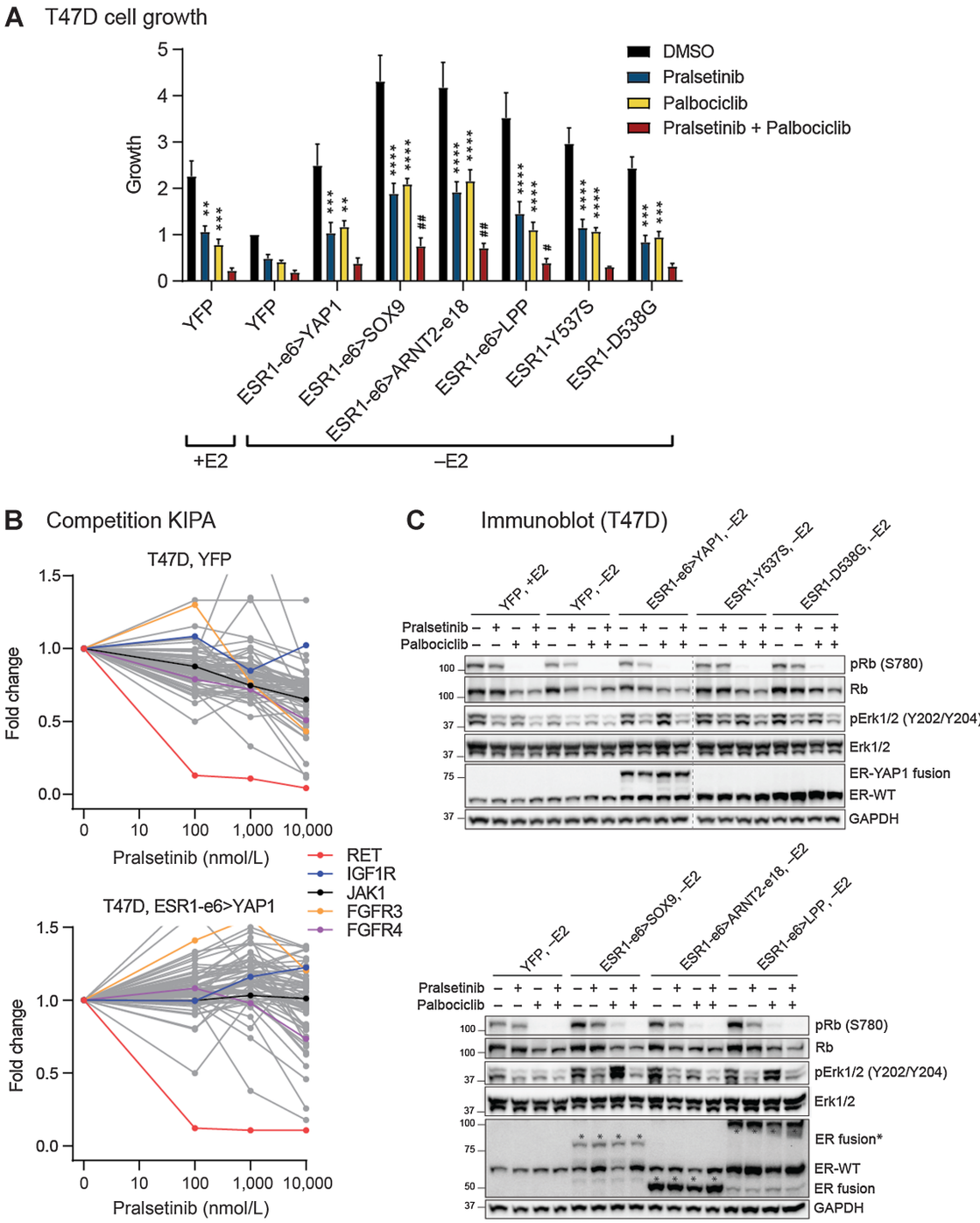

Figure 2.

RET and CDK4/6 inhibitors suppress ERα^{+} breast cancer cell growth driven by active ESR1 fusion proteins. **A,** Cell growth was assayed in E2-deprived stable cells by an alamarBlue assay (mean ± SEM, $n = 3$). Growth reading values were normalized to that of hormone-deprived YFP control cells in the vehicle (+DMSO) group. Two-way ANOVA followed by the Tukey test was used for multiple comparisons for each stable cell line after 500 nmol/L pralsetinib, 100 nmol/L palbociclib, or combination treatment in the presence or absence of 10 nmol/L E2. Single agent alone compared with DMSO. **, $P < 0.01$; ***, $P < 0.001$; ****, $P < 0.0001$. Combinatorial treatment compared with pralsetinib alone. #, $P < 0.05$; ##, $P < 0.01$. **B,** Competition KIPA was performed on lysates from T47D cells expressing YFP or ESR1-e6>YAP1 fusion protein treated by DMSO (vehicle) or increasing concentrations of pralsetinib (100 nmol/L, 1 μmol/L, and 10 μmol/L) for 30 minutes. **C,** Immunoblotting of lysates made from E2-deprived T47D cells stably expressing different ESR1 fusions/LBD mutants treated with DMSO, 500 nmol/L pralsetinib, 100 nmol/L palbociclib, or both pralsetinib and palbociclib for 48 hours. GAPDH served as a loading control. The dashed line indicates two separate blots that were conducted at the same time. The representative image is based on two independent experiments.

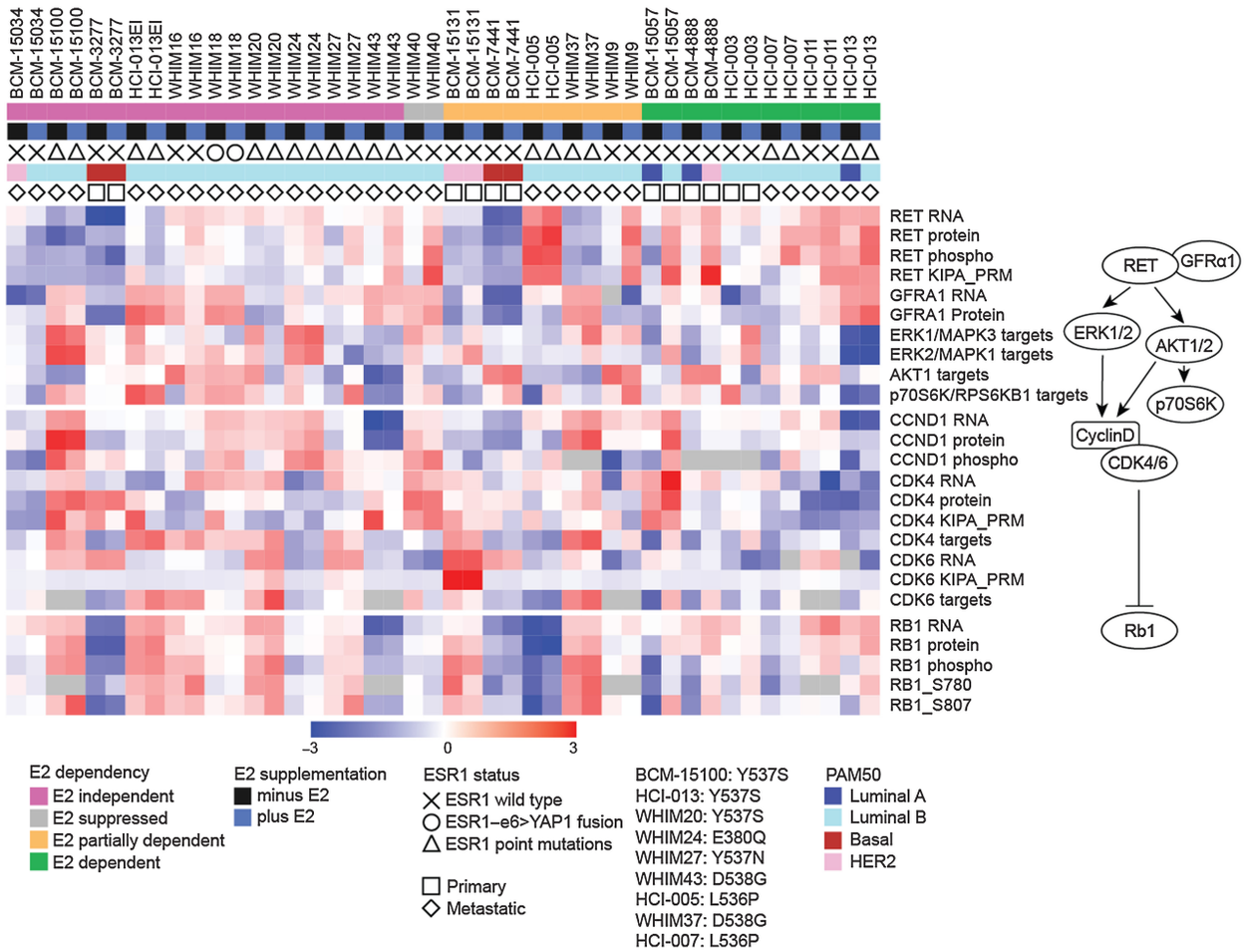

Figure 3.

Proteogenomic profiling identifies ERα$^+$ PDX models for RET and CDK4/6-directed therapy. Heatmap shows the proteogenomic characterization of kinase targets and cell-cycle–related mRNA and protein expression levels in 22 ERα$^+$ PDX models. Scale bar indicates row Z scores for RNA level (based on $\log_2$ ratio of RNA-seq data), for protein level (based on $\log_2$ ratio after TMT labeling/MS; see Materials and Methods), for phosphoprotein level [based on $\log_2$ ratio after TMT labeling after immobilized metal affinity chromatography (IMAC) enrichment/MS; see Materials and Methods], kinase level (based on KIPA $\log_{10}$ ratio), "targets" were defined from normalized enrichment scores of kinase targets from single sample post-translational modification signature enrichment analysis (13). The diagram on the right depicts RET/GFRA1 signaling pathway that promotes cell growth. The bottom legend informs on whether PDX tumor growth was affected by exogenous E2 given to the ovariectomized mice (colored squares), as well as whether E2 was supplemented in drinking water to mice (black and blue squares). It also states whether the PDX was established from a primary tumor or metastatic lesion and also the genomic status of the *ESR1* gene (either being wild type, bearing a point mutation or fusion).

Proteogenomics

Proteogenomics was performed as previously described (12–14). Frozen ERα$^+$ PDX tumors were cryopulverized with a Covaris CP02 Pulverizer. DNA was isolated using a QIAamp DNA Mini Kit (QIAGEN, cat# 51304) and total RNA using the RNeasy kit (QIAGEN), followed by sequencing performed at the Human Genome Sequencing Center at BCM as described previously (7). Tools, including Strelka2, Mutect2, and CARNAC (v 0.2.5b9), were used to detect somatic *ESR1* LBD gene variants. For RNA-seq analysis, paired-end 150 bp reads were aligned to the hg19 (GRCh37) reference genome using RSEM v1.2.31 (RSEM, RRID:SCR_013027; ref. 19) and Bowtie 2 (20). Protein was extracted in an 8 mol/L urea buffer with sonication and protein concentration was measured by Bradford assay.

Tandem mass tag quantitative proteomics and phosphoproteomics

Tandem mass tag (TMT) labeling of peptides and LC/MS analysis was performed as described in the CPTAC workflow (21) as implemented at National Cancer Institute for proteogenomics study.

Labeling of peptides using TMT11

Ten peptide samples from patients' tissue and one Common Reference (mixed peptides from all samples), as a plex, were labeled with TMT11 (Thermo Fisher Scientific, cat# A37725) as described previously (21, 22). Desalted and dried peptides from each sample were reconstituted in 100 µL 50 mmol/L HEPES, pH 8.5. The peptide concentration was determined using an A_{280} Nanodrop assay. 0.8 mg of each channel in the TMT11 panel was dissolved in 41 µL anhydrous

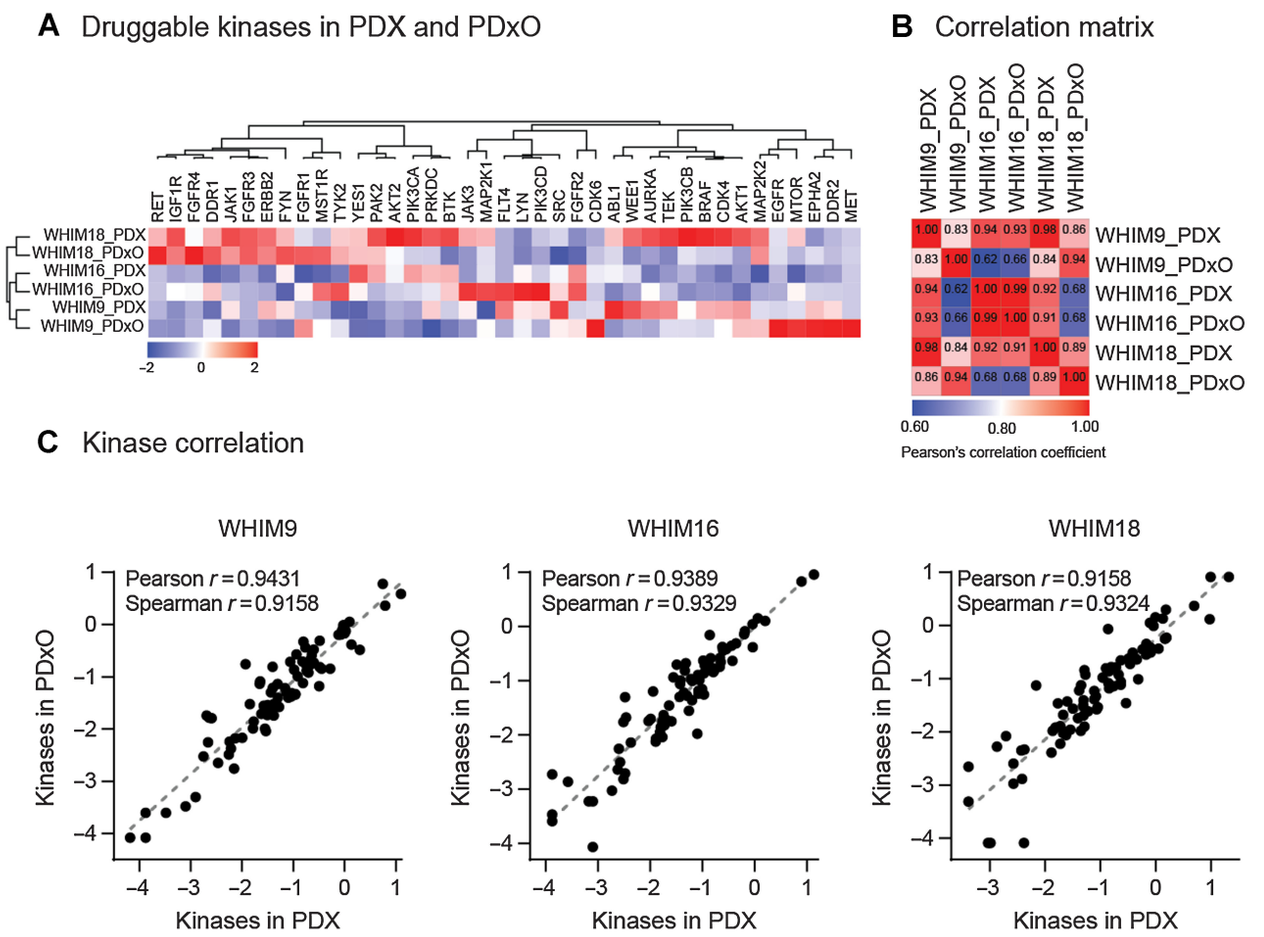

Figure 4.

Three ERα^{+} PDxO models recapitulate the kinome profile observed in matching PDX tumors. **A,** Heatmap showing the expression level of 39 druggable kinases in PDxO and PDX tumors. Kinase expression values were $\log_2$ transformed. Scale bar, row Z scores. Columns and rows were clustered using one minus Spearman rank correlation distance and complete linkage. **B,** Correlation matrix illustrating quantitative kinome correlations for PDX tumors, compared with their counterpart PDxO models. Color scale indicates Pearson correlation coefficient. **C,** Individual kinases (represented by the 88 dots) were highly correlated in PDX and PDxO models. Expression values were $\log_{10}$ transformed.

acetonitrile (ACN). TMT solution was mixed with 100-µg peptide aliquots and incubated on the shaker at room temperature for 1 hour. TMT-peptide conjugation was validated for quality control using single-shot LC-MS analysis on each labeled sample to ensure >99% labeling efficiency. Eight µL of 5% hydroxylamine was added to labeled peptides and mixed on the shaker at room temperature for 15 minutes to quench the conjugation reaction. Labeled peptides from all TMT channels were combined, dried, reconstituted with 1 mL 3% ACN/0.1% FA, desalted using a Sep-Pak C18 1cc Vac Cartridge (WAT054955), frozen at −80°C, and lyophilized.

bRPLC fractionation

An Agilent 1200 HPLC was used for offline basic reverse-phase liquid chromatography (bRPLC) fractionation. Basic setup for the HPLC separation includes mobile phase A [4.5 mmol/L ammonium formate ($HCOONH_3$)/2% ACN], mobile phase B [4.5 mmol/L ammonium formate ($HCOONH_3$), pH10/90% ACN], Agilent Zorbax 300 Extend-C18 column (3.5 µm, 4.6×250 mm), and a fraction collector that was set to collect at 1 fraction/min. The combined labeled peptide mixture (∼1.1 mg) was reconstituted with 420 µL 4.5 mmol/L ammonium formate ($HCOONH_3$) pH10/ 2% ACN. 400 µL of labeled peptides was injected onto the offline HPLC and elution was set at a flow rate of 1 mL/min. The HPLC analysis used a multistep linear gradient starting at 0% mobile B at 0 minutes, 16% mobile B at 13 minutes, 40% mobile B at 73 minutes, 44% mobile B at 77 minutes, 60% mobile B at 82 minutes, 60% mobile B till 96 minutes. The 96 collected fractions were combined and reduced to 25 fractions. Five percent (∼150 µL) of each fraction was aliquoted for global proteome LC/MS analysis. The remainder from 25 fractions were pooled once more and reduced to 13 fractions for phosphoproteomic analysis.

Phosphoproteomic enrichment

Labeled phosphopeptides were enriched using Fe-NTA IMAC beads, which were freshly prepared from Superflow Ni-NTA IMAC agarose beads (Qiagen, cat# 30410). Stage tips, which were packed with C18 solid-phase extraction disks (47-mm dia., 20 pack, Empore, cat# 66883-U) and conditioned with MeOH (2 × 100 µL), 50% ACN/ 0.1% FA (50 µL), 1% FA (2 × 100 µL), were used to recover bound phosphopeptides from Fe-NTA beads. Thirteen labeled peptides fractions were frozen, dried, and reconstituted in 80% ACN/ 0.1%TFA

and incubated with Fe-NTA beads for 30 minutes at room temperature on an end-over-end rotator. After incubation, Fe-NTA beads were washed with 80%ACN/ 0.1%TFA (2×50 μL), 1%FA (50 μL); and phosphopeptides were eluted from stage-tips with 500 mmol/L K_2HPO_4 elution buffer (3×70 μL), 1%FA (100 μL), and 50%ACN/ 0.1%FA (2×60 μL). These eluted fractions were frozen, dried, and reconstituted with 15 μL 3%ACN/0.1%FA for phosphoproteome analysis.

LC/MS analysis

Global proteome and phosphoproteome were analyzed using the Orbitrap Fusion Lumos Tribrid Mass Spectrometer coupled with EASY-nLC 1200 system (Thermo Fisher Scientific). The NanoLC column was prepared using PicoFrit fused silica tubing (360 μm OD x 75 μm ID), which was packed with ReproSil-Pur (120 Å, C18-AQ, 1.9 μm) resin (Dr. Maisch, cat# r119.aq). The NanoLC column was heated to 60°C using Phoenix Nanospray column heater (cat# mPST-CH-20U and controller Cat # PST-CHC). NanoLC separation used mobile phase A (3%ACN/0.1%FA), mobile phase B (90%ACN/0.1%FA), flowrate settings of 200 nL/min (0–100 min) and 500 nL/min (101–110 min), and a 110 minutes chromatography gradient that started at 2% mobile B at 0 minutes, 6% mobile B at 1 minute, 30% mobile B at 85 minutes, 60% mobile B at 94 minutes, 90% mobile B at 95 minutes, 90% mobile B at 100 minutes, 50% mobile B at 101 minutes, and 50% mobile B at 110 minutes.

Settings for data acquisition on the Orbitrap Fusion Lumos Tribrid Mass Spectrometer include positive ion mode, 300°C ion transfer tube temperature, 60,000/50,000 resolution setting for MS1/MS2, respectively, 4E5 for AGC target, 350–1800 *m/z* ion scan range, 0.7 *m/z* for isolation window, HCD energy of 38%, charge state isolation to include all ions with 2–6 charge states, 2 seconds for scanning duty cycle, and data acquisition in profiling mode.

Proteomic quantification

RAW MS files were converted into open mzML format using the MSConvert utility of the Proteowizard software suite (23). MS/MS spectra were searched and further processed using the FragPipe (v17.0) software (https://github.com/Nesvilab/FragPipe). MS/MS spectra were searched against a combined *Homo sapiens* (Uniprot ID: UP000005640) and *Mus musculus* (Uniprot ID: UP000000589) protein sequence database appended with an equal number of decoy sequences and common contaminants. Precursor-ion mass tolerance was set as 20 ppm and fragment mass tolerance was set as 0.02 Da and C12/C13 isotope errors (0/1/2/3) were allowed. Cysteine carbamidomethylation (+57.021460), lysine TMT labeling (+229.162932), and peptide N-terminal TMT labeling (+229.162932) were specified as fixed modifications. Methionine oxidation (+15.994900) and phosphorylation (+79.966331) of serine, threonine, and tyrosine residues were specified as variable modifications. Strict-trypsin was used as the digestion enzyme and allowed up to 2 missed cleavages. In each TMT 11-plex, the PSM lists were rescored using Percolator incorporated in FragPipe and additionally processed using PTMProphet to localize the phosphorylation sites. The protein groups were assembled by ProteinProphet. TMT-Integrator was used to generate summary reports at the phosphorylated site level. All the PSMs were filtered using a stringent, sequential FDR strategy, retaining only the PSMs with PeptideProphet probability of 0.9 or higher (which in these data corresponded to less than 1% PSM-level FDR). Confidently phosphorylated sites were defined as sites with PTMProphet localization probability larger than 0.75. Median centering was used to normalize the site abundance level quantification results. Finally, the median centering single site abundance level quantification table was used for the downstream analysis.

Pathway enrichment analysis

Phosphosite-level data were used for PTM signature enrichment analysis (24) to generate sample scores for kinase targets shown in **Fig. 3**.

Statistical analysis

ANOVA was performed with GraphPad Prism 9 (GraphPad Prism, RRID:SCR_002798), as indicated in the figure legends. *P* values less than 0.05 were considered statistically significant. The IC_{50} value concentrations were calculated by nonlinear regression [curve fit; log(inhibitor) vs. normalized response] using GraphPad Prism 9. Correlation was calculated using GraphPad Prism 9. Heatmaps were generated and unsupervised hierarchical clustering was performed using Morpheus (https://software.broadinstitute.org/morpheus; Morpheus, RRID:SCR_014975).

Data availability

Raw proteomics data from T47D cells and from ERα^+ PDX tumors in this study were deposited to the ProteomeXchange Consortium via the PRIDE (25) partner repository with the dataset identifiers PXD033339 and PXD036644, respectively. Raw whole exome sequencing/transcriptomics data from ERα^+ PDX tumors in this study are available in the database of Genotypes and Phenotypes (dbGaP) under accession number phs003324 (BioProject accession number PRJNA986276). All other raw data are available upon request from the corresponding author.

Results

ESR1-TAFs upregulate druggable kinase protein levels in a hormone-independent manner

To profile kinase levels in response to expression of a particular ESR1 fusion protein efficiently, a proteomic assay called KIPA was deployed (bioRxiv 2022.10.13.511593), whereby 5–9 different small-molecule kinase inhibitors were coupled to sepharose beads for enrichment of kinases from native cell or tumor lysates after pulldown, followed by MS for identification and quantification. T47D cell lysates expressing in-frame ESR1 fusions detected in samples from patients with metastatic breast cancer were assayed initially. Stable cell lines transduced with lentivirus expressing yellow fluorescent protein (YFP), truncated *ESR1* exon 6 (encoding an ESR1-e6 protein), and wild-type ERα (ESR1-WT) protein were included as negative controls and activating ESR1 LBD point mutants (Y537S and D538G) as comparison. The abundance of multiple receptor tyrosine kinases (RTK), including FLT4, RET, IGF1R, FGFR3, FGFR4, and MET, as well as the non-RTKs JAK1, AURKA, SRC, MAP2K2, ABL2, and TYK2 were significantly increased in T47D cells expressing ESR1-TAFs that we previously reported (7). These TAFs include ESR1-e6>YAP1, ESR1-e6>SOX9, ESR1-e6>LPP, ESR1-e6>ARNT2 (exon 2 and exon 18 fusions), ESR1-e6>TNRC6B, ESR1-e6>PCDH11X, ESR1-e6>GRIP1, ESR1-e6>CLINT1, and ESR1-e6>NCOA1 (**Fig. 1A**). The level of these kinases was also increased when constitutive activating ERα LBD point mutants, ESR1-Y537S and ESR1-D538G, were expressed (**Fig. 1A**). Other ESR1 fusions known to be transcriptionally weak or inactive (ESR1-e6>GYG1, ESR1-e6>TCF12, ESR1-e6>DAB2, ESR1-e6>PCMT1, and ESR1-e6>ARID1B; ref. 7) did not induce the expression of the above cited kinases (**Fig. 1A**). RET, JAK1, IGF1R, and FLT4 were the most significantly upregulated kinases in T47D cells

expressing active ESR1 fusions and point mutations compared with those expressing inactive fusions and controls ($P < 0.01$, fold change>2; Supplementary Fig. S1). The levels of RET, IGF1R, JAK1, FGFR3, and FGFR4 in these experiments were orthogonally validated using immunoblotting (**Fig. 1B**). Kinases that have an FDA-approved inhibitor were subject to subsequent pharmacological experiments.

Inhibition of RET and cyclin-dependent kinases 4 and 6 suppresses ESR1-TAF–driven cell growth

To examine responses to the inhibition of the above kinases *in vitro*, we tested the effects of kinase inhibitors directed against each kinase on the various T47D cell lines described above. Ganitumab, an anti-IGF1R antibody, was ineffective in inhibiting active ESR1 fusion-driven cell growth even at 1,000 μg/mL (Supplementary Fig. S2). Ruxolitinib, a pan-JAK inhibitor, and erdafitinib, a pan-FGFR inhibitor, suppressed cell growth at clinically nonachievable concentrations (>1 μmol/L; Supplementary Fig. S2). However, pralsetinib (BLU-667), an FDA-approved RET inhibitor for advanced RET-altered thyroid cancers and non–small cell lung cancer (NSCLC; ref. 26), revealed a significant reduction in the T47D *in vitro* growth induced by the ESR1-TAFs as well as the two ERα LBD mutants (Y537S, D538G; **Fig. 2A**). These data suggest that, despite marked diversity in the 3′ partner gene sequences, elevated RET kinase abundance is a common therapeutic vulnerability in ESR1-TAF–expressing breast cancer cells. To confirm that pralsetinib was selectively inhibiting RET, "competition KIPA" was performed whereby pralsetinib was added to cell lysates to compete for RET binding to the KIPA beads. Highly selective inhibition of RET protein binding was observed with the addition of pralsetinib, with a biochemical IC_{50} value of 14.1 nmol/L in YFP control lysates and 13.7 nmol/L in ESR1-e6>YAP1–expressing cell lysates (**Fig. 2B**).

Palbociclib, an FDA-approved cyclin-dependent kinases 4 and 6 (CDK4/6) inhibitor for treating patients with ERα$^+$ advanced breast cancer (10), reduced the growth of YFP control cells treated with E2 and ESR1-e6>YAP1 as previously reported (1). Similar effects were observed for cells expressing the ESR1-TAFs (SOX, ARNT2, and LPP) and the two ERα LBD point mutants (**Fig. 2A**). When pralsetinib was combined with palbociclib, growth of all cells was further reduced, with growth driven by ESR1-e6>SOX9, ESR1-e6>ARNT2-e18, and ESR1-e6>LPP being significantly decreased (**Fig. 2A**). Immunoblotting confirmed the expected inhibition of phosphorylation of the MAP kinases Erk1/2 (at Y202/Y204) and phosphorylation of the Retinoblastoma protein (Rb; at S780), the known downstream targets of activated RET and CDK4/6, respectively (**Fig. 2C**). Growth-inhibitory effects by pralsetinib were verified in MCF7 cells expressing ESR1-TAFs (Supplementary Fig. S3). Additive inhibition upon palbociclib treatment was also observed in MCF7 cells expressing ESR1 fusions.

Proteogenomic profiling identifies ERα$^+$ PDX models for RET and CDK4/6-directed therapy

We previously used genomics and transcriptomics to annotate a panel of 20 distinct ERα$^+$ PDX tumors exhibiting a variety of dependencies on E2 for growth (7). Additional proteomic and phosphoproteomic profiling was performed using TMT labeling and phosphoenrichment. The TMT11plex enabled identification and relative quantification of proteins using tandem MS. An analysis of these data revealed the distribution of therapeutic targets in 22 biologically heterogeneous ERα$^+$ PDX tumors. The ESR1-e6>YAP1–expressing WHIM18 PDX (27) demonstrated moderately high levels of RET and phospho-RET (upper 50% percentile) as well as of downstream ERK and AKT signaling and CDK4/6, cyclin D1 (CCND1) and phospho-Rb (phospho-RB1, upper 50% percentile; **Fig. 3**; Supplementary Fig. S4). Interestingly, WHIM18 PDX had high expression of GFRα-1 (GFRA1, in upper 25% percentile), a RET coreceptor (**Fig. 3**; Supplementary Fig. S4; ref. 28). As a comparison, the WHIM9 PDX line, which expresses WT ERα and showed partial sensitivity to E2 deprivation (7) has a relatively low level of RET (lower 50% percentile), but the expression of RET mRNA and protein was highly E2 induced (upper 25% percentile), as expected, given that *RET* is directly transcriptionally regulated by ERα (**Fig. 3**; Supplementary Figs. S4 and S5A; refs. 29, 30). The human *RET* gene encodes two major isoforms resulting from alternative splicing (31) and some ERα$^+$ PDXs displayed more alternative splicing isoform than others (Supplementary Fig. S5A). Like WHIM9, the growth of WHIM37 PDX tumors expressing ERα D538G

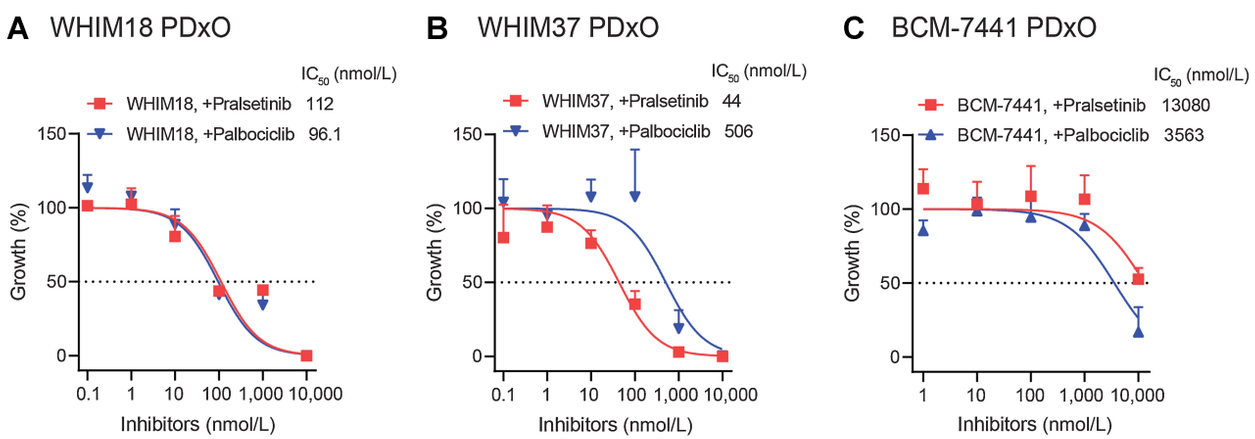

Figure 5.
RET and CDK4/6 inhibition suppresses ESR1 fusion-driven PDxO growth. **A,** WHIM18 PDxOs were plated in Matrigel as described previously in the Materials and Methods. DMSO or increasing doses of pralsetinib and palbociclib (0.1 nmol/L–10 μmol/L) were added and after one-to-two weeks, the inhibition of organoid growth was quantified using a CellTiter-Glo 3D cell viability assay (mean ± SEM, $n = 3$). **B** and **C,** The growth of WHIM37 (**B**) and BCM-7441 (**C**) PDxOs was measured as described in **A** (mean ± SEM, $n = 3$). PDxO growth reading values were normalized to that of DMSO vehicle.

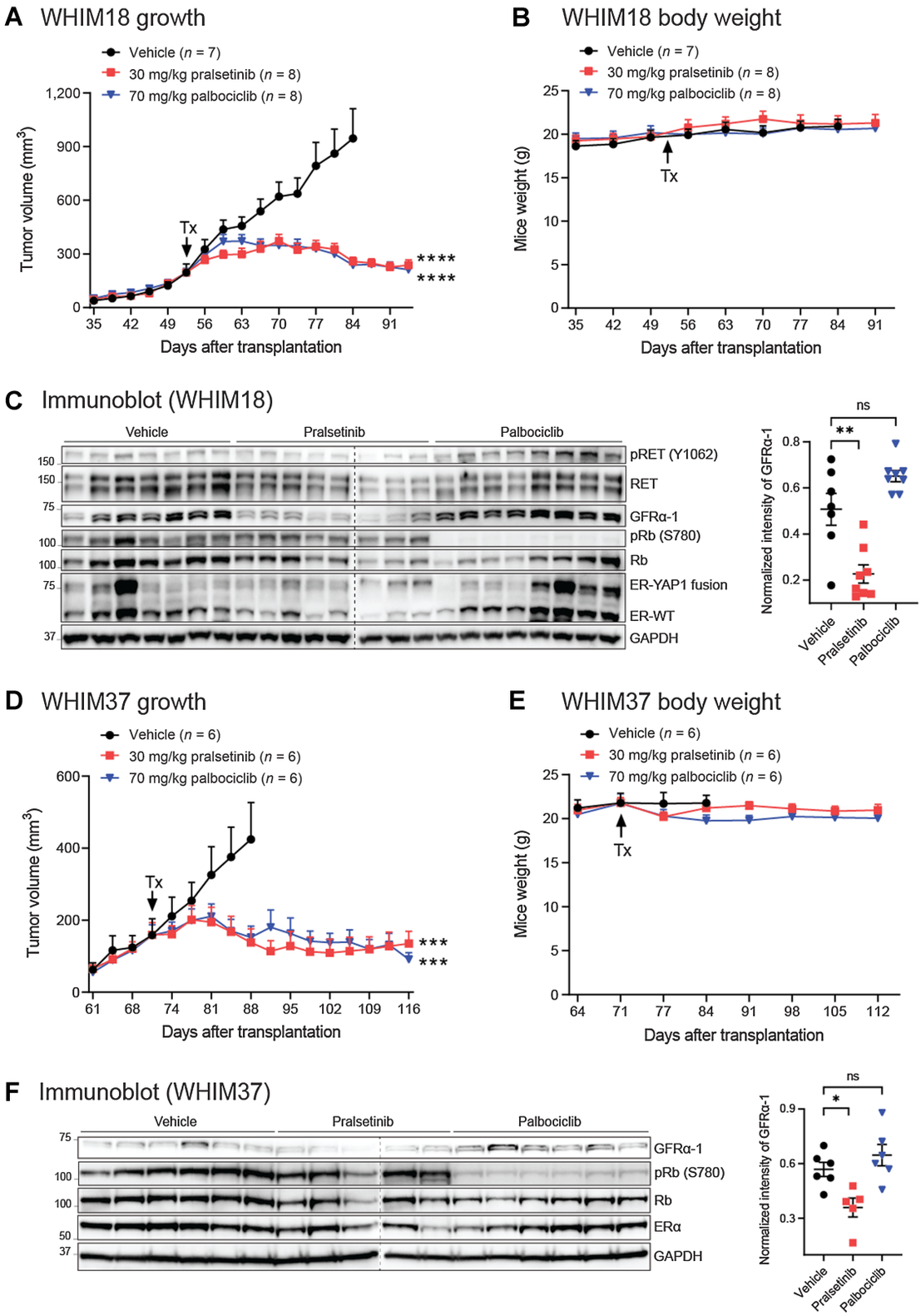
A WHIM18 growth
Vehicle (n = 7)
30 mg/kg pralsetinib (n = 8)
70 mg/kg palbociclib (n = 8)
Tumor volume (mm3)
Tx
****
****
Days after transplantation
B WHIM18 body weight
Mice weight (g)
Tx
Days after transplantation
C Immunoblot (WHIM18)
Vehicle
Pralsetinib
Palbociclib
pRET (Y1062)
RET
GFRα-1
pRb (S780)
Rb
ER-YAP1 fusion
ER-WT
GAPDH
Normalized intensity of GFRα-1
ns
**
Vehicle
Pralsetinib
Palbociclib
D WHIM37 growth
Vehicle (n = 6)
30 mg/kg pralsetinib (n = 6)
70 mg/kg palbociclib (n = 6)
Tumor volume (mm3)
Tx
***
***
Days after transplantation
E WHIM37 body weight
Vehicle (n = 6)
30 mg/kg pralsetinib (n = 6)
70 mg/kg palbociclib (n = 6)
Mice weight (g)
Tx
Days after transplantation
F Immunoblot (WHIM37)
Vehicle
Pralsetinib
Palbociclib
GFRα-1
pRb (S780)
Rb
ERα
GAPDH
Normalized intensity of GFRα-1
ns
*
Vehicle
Pralsetinib
Palbociclib

was partially E2-dependent (7). Although it had a low level of RET (lower 50% percentile), the expression of its coreceptor GFRA1 was high (upper 25% percentile, **Fig. 3**; Supplementary Fig. S4). WHIM43 PDX line that also carried the ESR1-D538G mutation expressed high levels of RET and GFRA1 but low levels of RB1, consistent with its previously reported loss (**Fig. 3**; ref. 32). The E2-independent line BCM-7441–expressing WT ERα showed basal levels of RET, GFRA1, and RB1 (in lower 25% percentile, **Fig. 3**; Supplementary Fig. S4), suggesting that ET resistance is independent of the RET pathway and Rb function.

Consistent with the above T47D cell line data, some other RTKs upregulated by ESR1-TAFs, including IGF1R, FGFR3, and FGFR4, were also increased in WHIM18 tumors as compared with other models; the RTK expression level was generally not induced by copy-number amplification (Supplementary Figs. S5B and S6). In fact, WHIM18 PDX tumors have a single-copy loss of the *RET* gene. The level of selected RTKs profiled by proteogenomics was validated by immunoblotting in WHIM9, WHIM18, WHIM20 (ESR1-Y537S), WHIM24 (ESR1-E380Q), WHIM27 (ESR1-Y537N), WHIM43, and WHIM16 (ESR1-WT; Supplementary Fig. S5A). Of note, the elevated level of RET, IGF1R, FGFR3, and FGFR4 observed in WHIM18 was mimicked in WHIM43 in the E2-deprived state (Supplementary Fig. S5A).

Our proteogenomic platform has demonstrated efficacy in predicting CDK4/6 inhibitor response in our ERα$^+$ PDX models. Concordant with the elevated levels of CDK4/6 and its downstream target Rb (**Fig. 3**), WHIM16, WHIM18, and WHIM20 tumors displayed reduced tumor growth when PDX mice were treated with palbociclib (1, 32, 33). Conversely, WHIM43, which displays low levels of the CDK4/6 signaling pathway (**Fig. 3**), demonstrated resistance to palbociclib (32). Therefore, we used these proteogenomic profiling data as the framework for designing subsequent pharmacological experiments.

Inhibition of RET and CDK4/6 suppresses ERα$^+$ PDX tumor growth

Human breast cancer PDX organoid (PDxO) models have been reported as a rapid approach to testing drug efficacy with high biological fidelity to their original tumors (16, 17). To test this hypothesis, organoid models were established from WHIM9, WHIM16, and WHIM18. These models were chosen to be representative of different E2 dependencies for tumor growth, *ESR1* mutation status and KIPA kinome profiles. WHIM18 naturally expresses the ESR1-e6>YAP1 fusion and demonstrates E2-independent growth (27). WHIM9 and WHIM16 express WT ESR1 and demonstrate E2-dependent and E2-suppressed growth, respectively (7). For the 39 druggable kinases detected by KIPA, the expression pattern in the PDxOs clustered with that of their parental PDX tumors (**Fig. 4A**). The kinome expression patterns (including 88 kinases beyond the 39 kinases considered druggable) showed a high degree of similarity between PDxO and PDX, with high Pearson's correlation coefficients based on three sets of matched pairs (**Fig. 4B**). The expression of individual kinases was also highly positively correlated between PDxO and originating PDX tumors with correlation coefficients (Pearson and Spearman) greater than 0.8 (**Fig. 4C**).

To explore response to kinase inhibition in the PDxOs, we evaluated the growth of WHIM18 PDxO in the absence or presence of increasing concentrations of pralsetinib or palbociclib. PDX cells were mixed with Matrigel and plated as organoid domes in 96-well plates for overnight before changing the culture media containing a 10-fold gradient concentration of respective drugs. After one-to-two weeks of treatment, organoid growth was quantified using a CellTiter-Glo 3D assay. The RET inhibitor decreased the growth of the WHIM18 PDxO, with an IC_{50} value comparable with CDK4/6 inhibition (∼100 nmol/L; **Fig. 5A**). As an additional method to measure WHIM18 PDxO growth, we transduced WHIM18 PDX cells with a lentivirus coexpressing GFP and firefly luciferase (Luc) and selected for tumor cells expressing GFP by FACS sorting. Cells from these GFP$^+$ tumors were also Luc$^+$, as expected. We then plated these WHIM18-Luc PDX cells as organoid domes. After drug treatment, luciferin was directly added to the organoid culture media and the growth was quantified using an IVIS imaging system to quantify photon release. By this assay palbociclib had an IC_{50} value of 25 nmol/L, whereas pralsetinib had an IC_{50} value of 120 nmol/L (Supplementary Fig. S7A). The growth of PDxO derived from WHIM37 (expressing low RET but high GFRA1, the RET coreceptor) was strongly inhibited by pralsetinib (IC_{50}: 44 nmol/L; **Fig. 5B**), indicating that either RET or GFRA1 could be sensitivity biomarkers for RET inhibition. As a negative control, PDxOs from BCM-7441, demonstrated to express both low RET and RB1, were resistant to both pralsetinib and palbociclib (**Fig. 5C**). Whether the combination of pralsetinib and palbociclib promotes additional WHIM18 PDxO growth inhibition versus either single agent was also tested. WHIM18 PDxOs were treated with either DMSO vehicle, single agents (pralsetinib or palbociclib) at less than their IC_{50} value concentrations or the combination of the two inhibitors. Although both single agents reduced PDxO growth as expected, no much further benefit was observed in the combination versus either single agent (Supplementary Fig. S7B).

We subsequently investigated the effectiveness of kinase inhibition on PDX tumor growth *in vivo*. WHIM18 PDX cells were injected subcutaneously into the fat pad of female SCID/beige mice and

Figure 6.

RET and CDK4/6 inhibitors suppress PDX tumor growth driven by an active ESR1 fusion (WHIM18) and LBD point mutant (WHIM37). **A,** Tumor volumes of WHIM18 PDX (mean ± SEM; *n* in each arm indicated) were measured daily. Arrow indicates the start of treatments (Tx), including vehicle, pralsetinib, or palbociclib containing chow diets. One-way ANOVA followed by the Tukey test was used to compare each treatment with vehicle arm. A *P* value denotes significance of tumor growth rates (slopes) derived from tumor volumes on the day of randomization to endpoint. **B,** Body weight of WHIM18 PDX mice. **C,** Left, Immunoblotting of RET, phospho-RET (Y1062), GFRα-1, Rb, phospho-Rb (S780), and ERα proteins in lysates made from different PDX tumors (vehicle, $n = 7$; pralsetinib, $n = 8$; palbociclib, $n = 8$). GAPDH served as a loading control. The dashed line indicates two separate blots that were conducted at the same time. Right, quantification of GFRα-1 protein. **D,** Tumor volumes of WHIM37 PDX (mean ± SEM; *n* in each arm indicated) were measured daily. Arrow, the start of treatments, including vehicle, pralsetinib, or palbociclib containing chow diets. One-way ANOVA followed by the Tukey test was used to compare each treatment to vehicle arm. A *P* value denotes significance of tumor growth rates (slopes) derived from tumor volumes on the day of randomization to endpoint. **E,** Body weight of WHIM37 PDX mice. **F,** Left, Immunoblotting of GFRα-1, Rb, phospho-Rb (S780), and ERα proteins in lysates made from different PDX tumors (vehicle, $n = 6$; pralsetinib, $n = 6$; palbociclib, $n = 6$). GAPDH served as a loading control. The dashed line indicates two separate blots that were conducted at the same time. Right, quantification of GFRα-1 protein. One-way ANOVA followed by the Tukey test was used. *, $P < 0.05$; **, $P < 0.01$; ***, $P < 0.001$; ****, $P < 0.0001$.

treatments were initiated when tumors reached approximately 200 mm^3. Treatments included vehicle (normal chow) or pralsetinib alone [60 mg/kg body weight (bw) per day in chow; ref. 26]. As a comparison with the current standard-of-care for ET-resistant patients, palbociclib alone (70 mg/kg bw per day in chow based on previous studies; ref. 1) was also examined, as well as the combination of both RET and CDK4/6 inhibition. Although pralsetinib alone and the combination treatment affected tumor growth of the WHIM18 PDX (Supplementary Fig. S8A), the mice body weight declined (Supplementary Fig. S8B), indicating that dosing at 60 mg/kg/d pralsetinib was toxic in the SCID/beige mouse model. To optimize the drug dose, half of the WHIM18 PDX mice on the palbociclib arm were given chow containing the combined kinase inhibitors every other day (60 mg/kg pralsetinib + 70 mg/kg palbociclib q.o.d., following 70 mg/kg palbociclib q.d. for two weeks). This dosing was not toxic as body weights were not reduced and revealed similar tumor reductions as compared with the standard 70 mg/kg/d palbociclib treatment arm (Supplementary Fig. S8A and S8B). Given the toxicity of 60 mg/kg pralsetinib and combination chow diets, the drug-containing chows were given to WHIM9 PDX mice every other day. The tumor volumes were also significantly suppressed by the RET inhibitor (Supplementary Fig. S8C), because the mice were not ovariectomized and producing endogenous E2, which will largely increase RET expression (**Fig. 3**). CDK4/6 inhibitor treatment showed similar WHIM9 tumor suppression as compared with RET inhibition. The combination of both inhibitors at the tested dosing did not reveal additional tumor reduction as compared with the single agents and the treated WHIM9 mice did not show any reduction of body weight (Supplementary Fig. S8C and S8D).

The *in vivo* study was subsequently repeated using a reduced pralsetinib dosing. Although tumor volumes of vehicle-treated WHIM18 PDX continued to increase, growth was significantly suppressed upon daily administration of pralsetinib at 30 mg/kg (**Fig. 6A**), with no apparent body weight loss (**Fig. 6B**). Palbociclib alone demonstrated a similar reduction in tumor volume (**Fig. 6A**). At the end of the study, pralsetinib-treated WHIM18 PDX tumors showed a decrease in RET phosphorylation (at Y1062) as well as a significant reduction in GFRα-1 protein expression (**Fig. 6C**). Palbociclib led to a reduction in the phosphorylation of Rb (S780), as expected. Pralsetinib (30 mg/kg) also displayed a significant reduction in tumor volume of WHIM37 PDX, without obvious body weight decrease (**Fig. 6D** and **E**). Protein expression of GFRα-1 was significantly reduced (**Fig. 6F**). In sum, our pharmacological experiments targeting RET or CDK4/6 validated proteogenomics-based predictions of drug response in all three tested ERα$^+$ PDX models.

Discussion

This study investigates the molecular basis and therapeutic vulnerabilities for *ESR1*-translocated tumors as well as *ESR1*-LBD–mutated tumors that have failed standard-of-care ET treatments. In contrast with previous efforts focused on the characterization of genomic and transcriptomic features of ERα$^+$ PDX (34, 35), herein we have focused on the utility of KIPA to profile the kinome of T47D ERα$^+$ breast cancer cells expressing distinct *ESR1* variants as well as 22 independent ERα$^+$ PDXs. The KIPA assay efficiently profiles kinase levels/activity in response to expression of an ESR1 fusion or point mutant using kinase inhibitors, chosen for broad kinase overage. The KIPA approach depletes interfering proteins and captures low concentration kinases that might be missed by global proteomics, thereby promoting sensitivity for profiling kinases and analyzing downstream pathways. We additionally deployed an integrated genomic, transcriptomic, and proteomic analysis of PDX models and matching PDxOs with an intent to model the prediction of drug sensitivities based on target and pathway expression. As PDXs represent a patient-authentic platform to understand underlying molecular mechanisms, establishment and investigation of PDxOs from human tumors facilitate the identification of predictive biomarkers and exploration of therapeutic targets. Our data revealed that a number of RTKs displayed reprogrammed elevated expression by ESR-TAFs with therapeutic potential, but only one, RET, was demonstrated to drive the growth promoted by active ESR1 fusions in cell lines, organoids derived from PDXs as well as the counterpart PDXs grown *in vivo*.

A core finding is that RET expression is activated in the presence of diverse active ESR1 fusions and LBD mutations. *RET* is a direct ERα target gene encoding an RTK that is upregulated in primary ERα$^+$ breast cancers (29, 36, 37). Activation of RET protein by its ligand glial cell line–derived neurotrophic factor stimulates intracellular MEK/ERK and PI3K/AKT kinase signaling pathways, thus promoting cell survival, proliferation, and migration (37, 38). Recent studies revealed RET as a potential therapeutic target in breast cancer. For example, targeting RET has been shown to sensitize breast cancer cells to aromatase inhibitors (AI) and tamoxifen (37, 39). Clinical trials have now evaluated the efficacy of multikinase inhibitors that display anti-RET activity, but results have not been promising. Vandetanib demonstrated no clinical benefit in pretreated patients with advanced breast cancer in a phase II trial. A greater number of patients progressed in the vandetanib plus docetaxel group compared with the placebo plus docetaxel group (40). When combined with the selective estrogen receptor degrader (SERD), fulvestrant, vandetanib also failed to improve progression-free survival and overall survival in ERα$^+$ breast cancer with bone metastases (41). In another phase II trial, cabozantinib had insufficient activity in patients with breast cancer with brain metastases (42). Sunitinib, either alone or in combination with chemotherapy, has no clinical benefit in improving survival outcomes for patients with advanced breast cancer (43). Possibilities for why these trials did not improve outcomes include: (i) Patients were not stratified using positive RET expression as a key criterion for patient inclusion; (ii) tumors might be driven by other mechanisms, like HER2 or FGFR amplification rather than dominated by RET; (iii) less-specific RET inhibitors were used (e.g., vandetanib also targets VEGFR, cabozantinib also targets MET and VEGFR, and sunitinib also targets VEGFR, PDGFR, and CSF1R); and (iv) off-target toxicity. These drugs have little selectivity in inhibiting RET over VEGFR2, pharmacologic targeting of which lead to adverse events, such as thrombosis, hypertension, and hemorrhage.

Praseltinib is a potent and highly selective RET inhibitor showing a favorable safety profile and tolerability compared with other multikinase inhibitors with RET-inhibitory activity and has been FDA-approved for metastatic thyroid cancer and NSCLC expressing activating RET mutants or fusions (26, 44). In our study, RET was constitutively induced by ESR1-TAFs expressed in T47D cells in an E2-independent manner. These data provided the initial premise to test the efficacy of this RET inhibitor. We have demonstrated the therapeutic potential of praseltinib in *ESR1* translocated breast cancer using ERα$^+$ breast cancer cell lines, PDxOs, and PDX mice models. Importantly, after dose optimization, treatments did not cause notable toxicity (based on lack of body weight loss) in tumor-bearing mice. We therefore speculate that RET inhibition will work similarly across ESR1-TAF–expressing tumors.

We also observed that praseltinib suppressed the growth of ERα$^+$ breast cancer cell lines, PDxOs and PDX tumors bearing *ESR1* LBD point mutations. WHIM37 PDX tumors (expressing ERα D538G) showed sensitivity to praseltinib, and these tumors expressed a high

GFRα-1 level but very low RET levels. The RET coreceptor GFRα-1 is canonically essential for RET activation (45, 46). However, it has been reported that GFRα-1 expression and internalization are RET-independent processes (47, 48). We previously found that *GFRA1* has elevated expression in ESR1-TAF–positive tumors, and it is one of 24 genes that compromise the MOTERA signature we have proposed to be diagnostic for *ESR1* mutation or translocation-driven tumors (7). Altogether, our data indicate that either RET or GFRα-1 could be a responsive marker to pralsetinib treatment in *ESR1* variant breast cancer tumors. These results potentially lay the framework for a clinical trial of pralsetinib in combination with AI or fulvestrant, the combination of palbociclib and pralsetinib, and palbociclib in combination with AI or fulvestrant or even an oral SERD with activity against ERα point mutants (e.g., elacestrant, ClinicalTrials.gov NCT03778931; camizestrant, ClinicalTrials.gov NCT04214288).

Pharmacological inhibition by praseltinib showed a similar tumor suppression to the CDK4/6 inhibitor palbociclib, providing a potential option for patients with advanced ERα$^+$ breast cancer expressing an active ESR1 fusion/mutant protein who have progressed on or developed resistance to CDK4/6 inhibition therapy. Although palbociclib combined with ET significantly increased progression-free survival of patients with advanced ER$^+$, HER2$^-$ breast cancer compared with those with ET alone, adverse events, especially neutropenia occurring in approximately 80% of patients compromised the treatment benefits (49–51). The lack of initial response to CDK4/6 inhibitors and the development of acquired resistance also commonly limited clinical outcomes (10, 49, 52). Various mechanisms have been reported to drive resistance to palbociclib, such as loss of Rb, increased expression of CDK6, amplification/overexpression of cyclin E1, and hyper-activating mutations in growth factor receptors (53). Resistance to RET inhibition has been reported to be mediated by mutations in the RET kinase domain (54) and activation of alternative kinase signaling (55). The convergent occurrence of these mechanisms may render resistance to the combination of palbociclib and pralsetinib. The clinical use of this selective RET inhibitor therefore demands further investigation in these settings.

In sum, our study highlights the utility of KIPA in defining targetable kinases overexpressed in *ESR1* translocated breast tumors and provides key preclinical evidence of RET as an actionable target for the treatment of ET-resistant, ESR1-TAFs expressing human breast tumors.

Authors' Disclosures

X. Gou reports grants from Cancer Prevention and Research Institute of Texas (CPRIT) during the conduct of the study, as well as reports a patent for MOTERA Signature pending. M. Anurag reports a patent for PCT/US2022/077924 pending. J.T. Lei reports a patent for MOTERA signature pending to Baylor College of Medicine. M. N. Young reports grants from Susan G. Komen Foundation, National Cancer Institute, U54CA233223, and National Cancer Institute, U01CA214125, during the conduct of the study. C.T. Vollert reports a patent for "Transcriptional reprogramming differentiates active from inactive ESR1 fusions in ET-refractory metastatic breast cancer" pending to Baylor College of Medicine. L.E. Dobrolecki reports personal fees from StemMed, Ltd. outside the submitted work. M.T. Lewis reports other support from StemMed Ltd., StemMed Holdings, and Tvardi Theraeutics Inc. outside the submitted work. S. Li reports personal fees from Inotiv, Inc. outside the submitted work. C.E. Foulds reports grants from Adrienne Helis Malvin Medical Research Foundation and DOD Breast Cancer Research Program during the conduct of the study; as well as other support from Coactigon, Inc., CoRegen, Inc., and Repare Therapeutics outside the submitted work; and reports a patent for PCT/US2022/077924 pending. M.J. Ellis reports personal fees from AstraZeneca during the conduct of the study and personal fees from Veracyte outside the submitted work; as well as reports a patent for PAM50 issued to Veracyte. No disclosures were reported by the other authors.

Authors' Contributions

X. Gou: Conceptualization, data curation, software, formal analysis, validation, investigation, visualization, methodology, writing–original draft, writing–review and editing. **B.-J. Kim:** Conceptualization, data curation, formal analysis, validation, investigation, methodology, writing–review and editing. **M. Anurag:** Data curation, software, formal analysis, investigation, methodology, writing–review and editing. **J.T. Lei:** Data curation, formal analysis, investigation, methodology. **M.N. Young:** Investigation, methodology, writing–review and editing. **M.V. Holt:** Investigation, methodology. **D. Fandino:** Investigation. **C.T. Vollert:** Formal analysis, investigation. **P. Singh:** Investigation. **M.A. Alzubi:** Investigation, methodology. **A. Malovannaya:** Investigation. **L.E. Dobrolecki:** Resources. **M.T. Lewis:** Resources, funding acquisition. **S. Li:** Resources. **C.E. Foulds:** Conceptualization, resources, data curation, supervision, funding acquisition, validation, investigation, writing–review and editing. **M.J. Ellis:** Conceptualization, resources, supervision, funding acquisition, project administration, writing–review and editing.

Acknowledgments

The authors gratefully acknowledge Drs. E.C. Chang and E.J. Jaehnig at Baylor College of Medicine for their scientific input and Dr. A.L. Welm at the University of Utah for help with HCI ER$^+$ PDX models. This work was supported by the following grants (to M.J. Ellis): Susan G. Komen Foundation (PG12220321, which supported J.T. Lei and M.J. Ellis; SAC190059, which supported M. Anurag, M.N. Young, and M.J. Ellis), National Cancer Institute (NCI) grants (P50CA186784, which supported B.-J. Kim, J.T. Lei, M. Anurag, M.T. Lewis, and M.J. Ellis, and U54CA233223 (to M.J. Ellis, which supported D. Fandino, P. Singh, C.T. Vollert, M.N. Young, M. Anurag, B.-J. Kim, and M.J Ellis), and as a CPRIT Scholar, a CPRIT Established Investigator Award (RR140033, which supported X. Gou, J.T. Lei, M. Anurag, and D. Fandino). The authors acknowledge funding from the DOD Breast Cancer Research Program Grant (W81XWH-21–1-0119 to M.J. Ellis and C.E. Foulds), which supported M. Anurag, D. Fandino, P. Singh, C.T. Vollert, B.-J. Kim, C.E. Foulds, and M.J. Ellis. They acknowledge the Adrienne Helis Malvin Medical Research Foundation through direct engagement with the continuous active conduct of medical research in conjunction with Baylor College of Medicine (M-2017 to C.E. Foulds, which supported him; M-2020 to M.J. Ellis and C.E. Foulds, which supported M. Anurag, P. Singh, C.T. Vollert, M.A. Alzubi, B.-J. Kim, C.E. Foulds, and M.J. Ellis). PDX mice work was also supported by U54CA224076 (to M.T. Lewis and A.L. Welm), which supported M.T. Lewis, and U54CA224083 (to S. Li), which supported him. X. Gou was also supported by a CPRIT training grant RP210027. J.T. Lei was also supported by a NIH training grant T32CA203690. The Baylor College of Medicine ER$^+$ PDXs were generated with a CPRIT Core Facility Support grant to CPRIT Scholar (to M.T. Lewis; RP170691, which supported L.E. Dobrolecki and M.T. Lewis) and P30 Dan L. Duncan Cancer Center Support grant (P30CA125123, which supported M.T. Lewis, A. Malovannaya, and M.J. Ellis). CPRIT Core Facility Awards (RP170005 and RP210227) and NIH High End Instrument Award (S10 OD026804) to the Baylor College of Medicine Mass Spectrometry Proteomics Core supported the work of A. Malovannaya. PDX proteogenomics was also supported by NCI U01CA214125 (to M.J. Ellis and M. Anurag), which supported M.V. Holt, A. Malovannaya, B.-J. Kim, P. Singh, C.T. Vollert, M.N. Young, M. Anurag, and M.J. Ellis. M.J. Ellis was also a Susan G. Komen Foundation Scholar and a McNair Scholar supported by the McNair Medical Institute at The Robert and Janice McNair Foundation.

The publication costs of this article were defrayed in part by the payment of publication fees. Therefore, and solely to indicate this fact, this article is hereby marked "advertisement" in accordance with 18 USC section 1734.

Note

Supplementary data for this article are available at Cancer Research Online (http://cancerres.aacrjournals.org/).

Received November 4, 2022; revised February 20, 2023; accepted April 12, 2023; published first April 18, 2023.

References

1. Lei JT, Shao J, Zhang J, Iglesia M, Chan DW, Cao J, et al. Functional annotation of ESR1 gene fusions in estrogen receptor-positive breast cancer. Cell Rep 2018;24:1434–44.
2. Hartmaier RJ, Trabucco SE, Priedigkeit N, Chung JH, Parachoniak CA, Vanden Borre P, et al. Recurrent hyperactive ESR1 fusion proteins in endocrine therapy-resistant breast cancer. Ann Oncol 2018;29:872–80.
3. Robinson DR, Wu YM, Lonigro RJ, Vats P, Cobain E, Everett J, et al. Integrative clinical genomics of metastatic cancer. Nature 2017;548:297–303.
4. Priestley P, Baber J, Lolkema MP, Steeghs N, de Bruijn E, Shale C, et al. Pan-cancer whole-genome analyses of metastatic solid tumours. Nature 2019;575:210–6.
5. Heeke AL, Elliott A, Feldman R, O'Connor HF, Pohlmann PR, Lynce F, et al. Molecular characterization of ESR1 variants in breast cancer. Breast Cancer Res Treat 2022;196:279–89.
6. Brett JO, Ritterhouse LL, Newman ET, Irwin KE, Dawson M, Ryan LY, et al. Clinical implications and treatment strategies for ESR1 fusions in hormone receptor-positive metastatic breast cancer: a case series. Oncologist 2023;28:172–9.
7. Gou X, Anurag M, Lei JT, Kim BJ, Singh P, Seker S, et al. Transcriptional reprogramming differentiates active from inactive ESR1 fusions in endocrine therapy-refractory metastatic breast cancer. Cancer Res 2021;81:6259–72.
8. Everolimus boosts endocrine therapy for breast cancer. Cancer Discov 2017;7:OF1.
9. Royce M, Bachelot T, Villanueva C, Ozguroglu M, Azevedo SJ, Cruz FM, et al. Everolimus plus endocrine therapy for postmenopausal women with estrogen receptor-positive, human epidermal growth factor receptor 2-negative advanced breast cancer: a clinical trial. JAMA Oncol 2018;4:977–84.
10. Turner NC, Slamon DJ, Ro J, Bondarenko I, Im SA, Masuda N, et al. Overall survival with palbociclib and fulvestrant in advanced breast cancer. N Engl J Med 2018;379:1926–36.
11. Pernas S, Tolaney SM. HER2-positive breast cancer: new therapeutic frontiers and overcoming resistance. Ther Adv Med Oncol 2019;11:1758835919833519.
12. Huang KL, Li S, Mertins P, Cao S, Gunawardena HP, Ruggles KV, et al. Proteogenomic integration reveals therapeutic targets in breast cancer xenografts. Nat Commun 2017;8:14864.
13. Krug K, Jaehnig EJ, Satpathy S, Blumenberg L, Karpova A, Anurag M, et al. Proteogenomic landscape of breast cancer tumorigenesis and targeted therapy. Cell 2020;183:1436–56.
14. Satpathy S, Jaehnig EJ, Krug K, Kim BJ, Saltzman AB, Chan DW, et al. Microscaled proteogenomic methods for precision oncology. Nat Commun 2020;11:532.
15. Zhang X, Claerhout S, Prat A, Dobrolecki LE, Petrovic I, Lai Q, et al. A renewable tissue resource of phenotypically stable, biologically and ethnically diverse, patient-derived human breast cancer xenograft models. Cancer Res 2013;73:4885–97.
16. Guillen KP, Fujita M, Butterfield AJ, Scherer SD, Bailey MH, Chu Z, et al. A human breast cancer-derived xenograft and organoid platform for drug discovery and precision oncology. Nat Cancer 2022;3:232–50.
17. Sachs N, de Ligt J, Kopper O, Gogola E, Bounova G, Weeber F, et al. A living biobank of breast cancer organoids captures disease heterogeneity. Cell 2018;172:373–86.
18. Duncan JS, Whittle MC, Nakamura K, Abell AN, Midland AA, Zawistowski JS, et al. Dynamic reprogramming of the kinome in response to targeted MEK inhibition in triple-negative breast cancer. Cell 2012;149:307–21.
19. Li B, Dewey CN. RSEM: accurate transcript quantification from RNA-seq data with or without a reference genome. BMC Bioinf 2011;12:323.
20. Langmead B, Salzberg SL. Fast gapped-read alignment with Bowtie 2. Nat Methods 2012;9:357–9.
21. Mertins P, Tang LC, Krug K, Clark DJ, Gritsenko MA, Chen L, et al. Reproducible workflow for multiplexed deep-scale proteome and phosphoproteome analysis of tumor tissues by liquid chromatography-mass spectrometry. Nat Protoc 2018;13:1632–61.
22. Navarrete-Perea J, Yu Q, Gygi SP, Paulo JA. Streamlined tandem mass tag (SL-TMT) protocol: an efficient strategy for quantitative (Phospho)proteome profiling using tandem mass tag-synchronous precursor selection-MS3. J Proteome Res 2018;17:2226–36.
23. Chambers MC, Maclean B, Burke R, Amodei D, Ruderman DL, Neumann S, et al. A cross-platform toolkit for mass spectrometry and proteomics. Nat Biotechnol 2012;30:918–20.
24. Krug K, Mertins P, Zhang B, Hornbeck P, Raju R, Ahmad R, et al. A curated resource for phosphosite-specific signature analysis. Mol Cell Proteomics 2019;18:576–93.
25. Perez-Riverol Y, Bai J, Bandla C, Garcia-Seisdedos D, Hewapathirana S, Kamatchinathan S, et al. The PRIDE database resources in 2022: a hub for mass spectrometry-based proteomics evidences. Nucleic Acids Res 2022;50:D543–D52.
26. Subbiah V, Gainor JF, Rahal R, Brubaker JD, Kim JL, Maynard M, et al. Precision targeted therapy with BLU-667 for RET-driven cancers. Cancer Discov 2018;8:836–49.
27. Li S, Shen D, Shao J, Crowder R, Liu W, Prat A, et al. Endocrine-therapy-resistant ESR1 variants revealed by genomic characterization of breast cancer–derived xenografts. Cell Rep 2013;4:1116–30.
28. Lo Nigro C, Rusmini M, Ceccherini I. RET in breast cancer: pathogenic implications and mechanisms of drug resistance. Cancer Drug Resist 2019;2:1136–52.
29. Stine ZE, McGaughey DM, Bessling SL, Li S, McCallion AS. Steroid hormone modulation of RET through two estrogen responsive enhancers in breast cancer. Hum Mol Genet 2011;20:3746–56.
30. Wang C, Mayer JA, Mazumdar A, Brown PH. The rearranged during transfection/papillary thyroid carcinoma tyrosine kinase is an estrogen-dependent gene required for the growth of estrogen receptor positive breast cancer cells. Breast Cancer Res Treat 2012;133:487–500.
31. Richardson DS, Rodrigues DM, Hyndman BD, Crupi MJ, Nicolescu AC, Mulligan LM. Alternative splicing results in RET isoforms with distinct trafficking properties. Mol Biol Cell 2012;23:3838–50.
32. Wardell SE, Ellis MJ, Alley HM, Eisele K, VanArsdale T, Dann SG, et al. Efficacy of SERD/SERM hybrid-CDK4/6 inhibitor combinations in models of endocrine therapy-resistant breast cancer. Clin Cancer Res 2015;21:5121–30.
33. Haricharan S, Punturi N, Singh P, Holloway KR, Anurag M, Schmelz J, et al. Loss of MutL disrupts CHK2-dependent cell-cycle control through CDK4/6 to promote intrinsic endocrine therapy resistance in primary breast cancer. Cancer Discov 2017;7:1168–83.
34. Olson JA Jr, Budd GT, Carey LA, Harris LA, Esserman LJ, Fleming GF, et al. Improved surgical outcomes for breast cancer patients receiving neoadjuvant aromatase inhibitor therapy: results from a multicenter Phase II trial. J Am Coll Surg 2009;208:906–14.
35. Ellis MJ, Suman VJ, Hoog J, Lin L, Snider J, Prat A, et al. Randomized Phase II neoadjuvant comparison between letrozole, anastrozole, and exemestane for postmenopausal women with estrogen receptor-rich stage 2 to 3 breast cancer: clinical and biomarker outcomes and predictive value of the baseline PAM50-based intrinsic subtype–ACOSOG Z1031. J Clin Oncol 2011;29:2342–9.
36. Esseghir S, Todd SK, Hunt T, Poulsom R, Plaza-Menacho I, Reis-Filho JS, et al. A role for glial cell-derived neurotrophic factor induced expression by inflammatory cytokines and RET/GFR alpha 1 receptor upregulation in breast cancer. Cancer Res 2007;67:11732–41.
37. Plaza-Menacho I, Morandi A, Robertson D, Pancholi S, Drury S, Dowsett M, et al. Targeting the receptor tyrosine kinase RET sensitizes breast cancer cells to tamoxifen treatment and reveals a role for RET in endocrine resistance. Oncogene 2010;29:4648–57.
38. Gattelli A, Nalvarte I, Boulay A, Roloff TC, Schreiber M, Carragher N, et al. Ret inhibition decreases growth and metastatic potential of estrogen receptor positive breast cancer cells. EMBO Mol Med 2013;5:1335–50.
39. Morandi A, Martin LA, Gao Q, Pancholi S, Mackay A, Robertson D, et al. GDNF-RET signaling in ER-positive breast cancers is a key determinant of response and resistance to aromatase inhibitors. Cancer Res 2013;73:3783–95.
40. Boer K, Lang I, Llombart-Cussac A, Andreasson I, Vivanco GL, Sanders N, et al. Vandetanib with docetaxel as second-line treatment for advanced breast cancer: a double-blind, placebo-controlled, randomized Phase II study. Invest New Drugs 2012;30:681–7.
41. Clemons MJ, Cochrane B, Pond GR, Califaretti N, Chia SK, Dent RA, et al. Randomised, Phase II, placebo-controlled, trial of fulvestrant plus vandetanib in postmenopausal women with bone only or bone predominant, hormone-receptor-positive metastatic breast cancer (MBC): the OCOG ZAMBONEY study. Breast Cancer Res Treat 2014;146:153–62.
42. Leone JP, Duda DG, Hu J, Barry WT, Trippa L, Gerstner ER, et al. A Phase II study of cabozantinib alone or in combination with trastuzumab in breast cancer patients with brain metastases. Breast Cancer Res Treat 2020;179:113–23.

43. Elgebaly A, Menshawy A, El Ashal G, Osama O, Ghanem E, Omar A, et al. Sunitinib alone or in combination with chemotherapy for the treatment of advanced breast cancer: a systematic review and meta-analysis. Breast Dis 2016; 36:91–101.
44. Markham A. Pralsetinib: first approval. Drugs 2020;80:1865–70.
45. Goodman KM, Kjaer S, Beuron F, Knowles PP, Nawrotek A, Burns EM, et al. RET recognition of GDNF-GFRalpha1 ligand by a composite binding site promotes membrane-proximal self-association. Cell Rep 2014;8:1894–904.
46. Leppanen VM, Bespalov MM, Runeberg-Roos P, Puurand U, Merits A, Saarma M, et al. The structure of GFRalpha1 domain 3 reveals new insights into GDNF binding and RET activation. EMBO J 2004;23:1452–62.
47. Vieira P, Thomas-Crusells J, Vieira A. Internalization of glial cell-derived neurotrophic factor receptor GFR alpha 1 in the absence of the ret tyrosine kinase coreceptor. Cell Mol Neurobiol 2003;23:43–55.
48. Bosco EE, Christie RJ, Carrasco R, Sabol D, Zha J, DaCosta K, et al. Preclinical evaluation of a GFRA1 targeted antibody–drug conjugate in breast cancer. Oncotarget 2018;9:22960–75.
49. Finn RS, Martin M, Rugo HS, Jones S, Im SA, Gelmon K, et al. Palbociclib and letrozole in advanced breast cancer. N Engl J Med 2016; 375:1925–36.
50. Rugo HS, Finn RS, Dieras V, Ettl J, Lipatov O, Joy AA, et al. Palbociclib plus letrozole as first-line therapy in estrogen receptor-positive/human epidermal growth factor receptor 2-negative advanced breast cancer with extended follow-up. Breast Cancer Res Treat 2019;174:719–29.
51. Lynce F, Blackburn MJ, Zhuo R, Gallagher C, Hahn OM, Abu-Khalaf M, et al. Hematologic safety of palbociclib in combination with endocrine therapy in patients with benign ethnic neutropenia and advanced breast cancer. Cancer 2021;127:3622–30.
52. Shah M, Nunes MR, Stearns V. CDK4/6 Inhibitors: game changers in the management of hormone receptor-positive advanced breast cancer? Oncology 2018;32:216–22.
53. Watt AC, Goel S. Cellular mechanisms underlying response and resistance to CDK4/6 inhibitors in the treatment of hormone receptor-positive breast cancer. Breast Cancer Res 2022;24:17.
54. Subbiah V, Shen T, Terzyan SS, Liu X, Hu X, Patel KP, et al. Structural basis of acquired resistance to selpercatinib and pralsetinib mediated by non-gatekeeper RET mutations. Ann Oncol 2021;32:261–8.
55. Nelson-Taylor SK, Le AT, Yoo M, Schubert L, Mishall KM, Doak A, et al. Resistance to RET-inhibition in RET-rearranged NSCLC is mediated by reactivation of RAS/MAPK signaling. Mol Cancer Ther 2017;16:1623–33.